Annealing temperature dependence of optical and structural properties of Cu films

Jiamin Liu, Meng Wang, Hao Jiang,* Jianbin Lin, Honggang Gu, Xiuguo Chen, Tielin Shi, and Shiyuan Liu†
State Key Laboratory of Digital Manufacturing Equipment and Technology, Huazhong University of Science and Technology, Wuhan 430074, China

(Received 5 September 2019; revised manuscript received 4 December 2019; published 17 January 2020)

Annealing temperature dependency of the optical and structural properties of Cu films is carefully studied using multiple means such as spectroscopic ellipsometry, x-ray diffraction, white-light interferometry, atomic force microscopy, scanning electron microscope (SEM), and the four-probe method. A wide annealing temperature range from 300 to 1200 K is examined experimentally. We find that the optical and structural properties of Cu films annealed at above 600 K cannot be naturally extended from the data commonly achieved on the samples annealed at the temperature below 600 K. When the annealing temperature is increasing, two transition points at around 600 and 900 K have been found by the Drude-Tauc-Lorentz analysis of the dielectric functions covering the energy range from 0.73 to 6.42 eV. The transition feature at 600 K can be attributed to the improvement of the crystalline state caused by annealing, which can be interpreted by the sharper diffraction peak shown in x-ray diffraction (XRD). The transition feature at 900 K was caused by the emergence of island structure due to the high-temperature annealing, which was supported by the SEM images as well. In fact, both the conspicuous scattering characteristics in the pseudodielectric function and the spurious peaks in the XRD pattern indicate the dramatically morphologic changes induced by the migration and reaggregation of Cu nanoparticles. The downward trend of dc resistivity captured in dielectric function analysis was supported by that of the sheet resistivity measured by the four-probe method.

DOI: 10.1103/PhysRevB.101.014107

I. INTRODUCTION

Annealing treatment is a process where material was heated to a specific temperature, held at the temperature for a certain time, and then cooled slowly to room temperature, which is desirable in many application [1–4]. Although an accurate choice of annealing temperature is rather difficult due to the lack of systematic studies of the influence caused by annealing, comprehensive studies on the effects of different annealing temperature on material properties can be found in literature. The differential electron densities and the local distortion of the ZrO_8 polyhedra in zirconia annealed at 873 and 1073 K have been investigated through experimental methods and first-principles calculations [5]. Nakashima *et al.* studied the regulations of magnetic properties for disordered zinc ferrite thin films via thermal annealing at 573, 673, and 1073 K, and they found that the magnetization was enhanced and then decreased with increasing of the annealing temperature [6]. Meškinis *et al.* have investigated the diamondlike carbon films with embedded Ag nanoparticles, which are annealed at 413, 473, 573, and 673 K [7]. It is worth noting that some studies have been implemented over a wider annealing temperature range to regulate the photoelectric properties of materials. The electric and optical properties of high-quality indium tin oxide thin films annealed at different temperature between 373 and 873 K are investigated by ellipsometry, spectrophotometry, and x-ray measurements [8]. The evolution of optical properties of Al-doped ZnO films annealed at different temperature is interpreted by spectroscopic ellipsometry [9], in which the annealing temperature of 673–973 K has been chosen to highlight the effects of the variation of free-electron concentration of the oxide films. Abdullin *et al.* present the evolutions of photoluminescence and electrical properties of boron-doped zinc oxide films, as a function of annealing temperature between 298 and 723 K, which can be attributed to the formation of acceptor levels induced by annealing [10]. However, the evolution of the dielectric property, the morphology, and structural property at higher annealing temperature is still not well understood. Moreover, the above studies rarely consider the correlation between photoelectric and morphological properties, which is necessary for the accurate analysis. To select an appropriate optical model to determine the dielectric functions, the morphology of material usually has to be considered [11]. Meanwhile, the evolution of crystal structural parameters is likely to cause changes in the properties of electronic structures [12,13]. Therefore, a comprehensive study on the influence of morphologic and crystalline structural changes caused by annealing process on the dielectric properties is highly desirable. Among the noble metals, the dielectric properties of Cu are particularly vital to be understood [14,15], because its dielectric properties are the basic knowledge for the widespread applications of Cu in the field of microelectronic devices [16], plasmonics [17], and photocatalysis [18]. At present, the study of dielectric properties of Cu is mostly limited to the direct measurement and theoretical calculation of as-deposited films [19], and the dielectric functions of annealed Cu are rarely reported.

*hjiang@hust.edu.cn
†shyliu@hust.edu.cn

In this paper, the dielectric functions of Cu films with nominal thickness of 100 nm annealed at different temperature from 300 to 1200 K are studied thoroughly. The Cu films are deposited on (100) single-crystal silicon substrate by direct-current magnetron sputtering and then are annealed in a tubular furnace in H_2 and Ar flow. Spectroscopic ellipsometry in the spectral range between 0.73 and 6.42 eV is employed to determine the dielectric functions of the annealed Cu films. The variation of dc resistivity, electron relaxation time, the absorption peaks, and the broadening parameters with the annealing temperature are analyzed based on the Drude-Tauc-Lorentz analysis. Meanwhile, white-light interferometry (WLI), atomic force microscopy (AFM), and scanning electron microscope (SEM) are used to characterize the surface and cross-section topography to study the evolution of morphology with the annealing temperature caused by the migration and reaggregation of Cu nanoparticles. X-ray diffraction (XRD) and four-probe resistivity experiments are carried out to determine the evolutionary structural properties and resistivity of Cu films, respectively. Results show that there exist two critical transition temperatures of 600 and 900 K for the annealed Cu films. At the former transition point, the dc resistivity and the electron scattering time exhibit the decrease trend and increase trend, respectively, which might be attributed to the change of crystalline state. Moreover, at the latter transition point, the electron scattering time sharply increases from 21 to 89 fs, and the plasmon properties become notable at about 2.0 eV with the formation of isolated islands.

II. MEASUREMENT AND METHOD

A. Sample preparation

The annealed Cu films were fabricated by a similar method described previously in Ref. [20]. First of all, Cu films were sputtered on the Si substrates from a pure Cu target (purity of 99.999%) by direct-current magnetron sputtering (TPR-450, China). The base pressure was 5×10^{-3} Pa, the distance between Cu target and Si substrate was about 35 cm, the sputtering power was set at a fairly low value of 50 W, and the rotating speed of the stage was 15 rev/min during the depositing. The sputtering was carried out in Ar (99.99% purity) plasma atmosphere under a working pressure of 0.3 Pa at 300 K to prohibit the sample being oxidized during sputtering. A presputtering process was introduced to remove oxides or other organic impurities from the surface of the Cu target. Specifically, the Si substrate was successively cleaned with acetone and ethanol in ultrasound for 5 min. Then, the substrate was rained with deionized water and dried with nitrogen flow. The Cu films with the thickness of 100 nm were obtained under a fixed deposition rate at 0.4 nm/s by setting the deposition time as 250 s. Then, the Cu films were annealed in a tubular furnace (GSL1400X, MTI Corporation Co., USA) immediately after the deposition of the Cu films. Prior to annealing, the furnace chamber was first vacuumed to a relative pressure of −0.1 MPa, and then a mixed flow with 5% H_2 and 95% Ar was injected into the chamber, in which the pressure would be a relative pressure of 0.04 MPa. After repeating the above operations three times in succession, the mixed flow with 5% H_2 and 95% Ar was injected into the chamber in which the pressure would be a relative pressure of 0.02 MPa, and then the annealing experiment was performed in the furnace chamber at different temperature from 400 to 1200 K with the step of 100 K. Such process can minimize the oxidation of the Cu film surface and ensure that the optical and structural properties of Cu films are measured instead of measuring CuO. The heating rate was 10 K/min and each annealing temperature was sustained for 1 h within the fluctuation of 5 K.

B. Characterization and calculation tools

The surface topography of each Cu film was characterized by the WLI and the AFM. Three root-mean-square roughness R_a in the microspot and S_a in the big spot were determined from the results reported by WLI (NewView 9000, Zygo Corporation Co., USA) and AFM (MultiMode 8, Bruker Corporation, USA), respectively. The sectional view of each annealed film was obtained by SEM (Helios NanoLab G3 CX, FEI Corporation Co., Czech Republic) to further study the morphological evolution with the annealing temperature. The thicknesses of the Cu films were determined as 99.5 nm through measuring the height difference of lithography stairs by profilometer (Veeco NT-1100 PROFILER, Oxford Corporation, UK). The phase composition and the crystallographic structural property of each film were investigated by XRD (PANalytical PW3040-60 MRD, Malvern Panalytical, Holland). The optical properties of the annealed Cu films were determined by spectroscopic ellipsometry measurement (ME-L, Wuhan Eoptics Technology Co., Wuhan, China) in the spectral range of 0.73 and 6.42 eV in steps of 0.01 eV, at angles of incidence setting as 60°, 65°, and 70°. The dielectric functions of Cu films were obtained based on Drude-Tauc-Lorentz analysis from a commercial analysis software (Eometrics, Wuhan Eoptics Technology Co., Wuhan, China) [20]. The sheet resistivity of the annealed films was measured via four-probe method.

Both the heating and annealing dynamics for the lattice parameters prediction were carried out via FORCITE package in the Material Studio. The COMPASS force field and the Ewald method are chosen to calculate the electrostatic interactions and van der Waals interactions. The heating dynamics calculation adopted the isothermal-isobaric ensemble with a Nosé thermostat and a Berendsen barostat. After the temperature setting as a value between 400 and 1200 K, the dynamics relaxation was first performed, and then the structure optimization was carried out to determine the heated structure. The annealing dynamics calculation adopted the isoenthalpic-isobaric ensemble with a Berendsen barostat. All the initial temperatures are set as 300 K, and the midcycle temperature is set as a value between 400 and 1200 K, and 5 cycles are computed with 1000 dynamics steps per cycle. After 5000 dynamics steps, the relaxed structure will be obtained.

C. Dielectric function determination

The ellipsometric parameters ψ and Δ, measured by ellipsometer, describe the ratio ρ of complex reflection coefficients r_p and r_s for p- and s polarization [21],

$$\rho = \tan(\psi)e^{i\Delta} = r_p/r_s. \quad (1)$$

Since the thickness of annealed Cu films is larger than the skin depth or the bulk electron mean-free path of the noble metals, the pseudodielectric function $\langle\varepsilon\rangle$ can be used to roughly describe the effective dielectric function of the sample [22],

$$\langle\varepsilon\rangle = \sin^2\theta_i\left[1+\tan^2\theta_i\left(\frac{1-\rho}{1+\rho}\right)^2\right], \tag{2}$$

where θ_i is the incidence angle.

The dielectric functions of each annealed Cu film were investigated thoroughly based on the Drude-Tauc-Lorentz analysis with roughness taken into account, which gives the insight to the electronic structure of samples. As for the Cu films annealed at temperature below 900 K, the optical model of the samples was created as a roughness layer on top of Cu substrate, where the dielectric function of Cu substrate is described by the Drude-Tauc-Lorentz layer. The corresponding model is shown as follows:

$$\varepsilon_{\mathrm{Cu}} = \frac{A_0}{-E^2} + \varepsilon_{\mathrm{Drude}} + \sum_{j=1}^{2}\varepsilon_{\mathrm{Tauc\text{-}Lorentz},j}, \tag{3}$$

where $\varepsilon_{\mathrm{Drude}}$ and $\varepsilon_{\mathrm{Tauc\text{-}Lorentz}}$ represent the intraband transitions of the free electrons and the interband transitions of the conduction electrons, respectively. A_0/E^2 is a Sellmeier infrared pole term added to the real ε_1 term to introduce dispersion in the infrared range [23]. A_0 is the amplitude of the infrared pole, and E is the energy of incident photons in the range between 0.73 and 6.42 eV. Specifically, the Drude term describes the dielectric response in the spectral range between near-infrared and the visible, which is given by [24]

$$\varepsilon_{\mathrm{Drude}} = \varepsilon_\infty - \frac{\hbar^2}{\varepsilon_0\rho_{\mathrm{dc}}(E^2\tau + i\hbar E)}, \tag{4}$$

where ε_∞ is the high-frequency dielectric constant caused by the effect of interband transition at high energy. ε_0 and $\hbar$ are the vacuum permittivity and the reducible Planck constant, respectively. ρ_{dc} is the dc resistivity of Cu film, and τ is the electron relaxation time. The correlation between the dc resistivity and the electron relaxation time is expressed as follows:

$$\rho_{\mathrm{dc}} = \frac{1}{N_e e\mu} = \frac{m^*}{N_e e^2\tau} = \frac{1}{\varepsilon_0\tau\omega_p^2}, \tag{5}$$

where N_{e} and μ are the concentration and the drift mobility of conduction electrons, respectively. e represents the electronic charge. m^* and ω_p are the electron effective mass and the plasma frequency, respectively.

The Tauc-Lorentz terms describe the dielectric functions of Cu films in the spectral range from visible and ultraviolet, where the asymmetric absorption-peak profile exists. It can be given by [25,26]

$$\varepsilon_{2,\mathrm{Tauc\text{-}Lorentz},j}(E) = \begin{cases} \frac{1}{E}\frac{A_j E_{\mathrm{peak},j} C_j (E-Eg_j)^2}{(E^2-E_{\mathrm{peak},j}^2)^2 + C_j^2 E_{\mathrm{peak},j}^2} & E > Eg_j \\ 0 & E \leqslant Eg_j \end{cases} \quad j=1,2, \tag{6}$$

$$\varepsilon_{1,\mathrm{Tauc\text{-}Lorentz},j}(E) = \frac{2}{\pi}P\int_{Eg_j}^{\infty}\frac{\xi\varepsilon_{2,\mathrm{Tauc\text{-}Lorentz},j}(\xi)}{\xi^2-E^2}d\xi, \tag{7}$$

where $\varepsilon_{1,\mathrm{Tauc\text{-}Lorentz},j}$ and $\varepsilon_{2,\mathrm{Tauc\text{-}Lorentz},j}$ represent the real part and imaginary part of the jth Tauc-Lorentz term, respectively. $\varepsilon_{1,\mathrm{Tauc\text{-}Lorentz},j}$ is derived from $\varepsilon_{2,\mathrm{Tauc\text{-}Lorentz},j}$ based on the Kramers-Kronig relations [21]. A_j, C_j, and $E_{\mathrm{peak},j}$ are the amplitude, the broadening parameter, and the position of the j^{th} absorption peak $\varepsilon_{2,\mathrm{Tauc\text{-}Lorentz},j}$. Eg_j stands for the corresponding optical band gap. P is the Cauchy principal value of the integral.

According to the Bruggeman effective medium approximation (BEMA) [27], the dielectric function of the roughness layer $\varepsilon_{\mathrm{eff}}$ can be described as follows:

$$\frac{\varepsilon_{\mathrm{Cu}}-\varepsilon_{\mathrm{eff}}}{\varepsilon_{\mathrm{Cu}}+2\varepsilon_{\mathrm{eff}}} + \frac{\varepsilon_{\mathrm{Air}}-\varepsilon_{\mathrm{eff}}}{\varepsilon_{\mathrm{Air}}+2\varepsilon_{\mathrm{eff}}} = 1, \tag{8}$$

where $\varepsilon_{\mathrm{Cu}}$ and $\varepsilon_{\mathrm{Air}}$ represent the dielectric function of the Cu film layer and the air, respectively. Meanwhile, the surface roughness is set as d_s.

As for the Cu films annealed at temperature above 900 K, the optical model of the sample was created as an effective Cu layer on top of Si substrate, where the dielectric function of effective Cu layer is still described by the Bruggeman effective medium approximation. In the Bruggeman effective medium approximation model, the dielectric functions of metallic phase are described as the combination of a Drude term, a Tauc-Lorentz term, two Lorentz terms, and an IR-pole term. When the annealing temperature is above 900 K, the morphology of Cu samples is gradually transformed from a continuous film into an island structure, which will be discussed in detail in the following sections. It should be noticed that the sizes of the Cu islands are comparable to the light wavelength, resulting in the possible inapplicability of BEMA [28,29]. Since the separating spacing between the Cu islands is larger than 100 nm, which makes the near-field coupling between islands ignorable [30], the presupposition for BEMA that the Cu islands are embedded in a homogeneous background field is still valid. In order to reduce the effect of Mie scattering caused by the Cu islands with the size comparable with the light wavelength, the spectral range of ellipsometric analysis was limited to below 2.9 eV.

The fitting coefficients in the above dielectric function model are d_s, A_0, ε_∞, ρ_{dc}, τ, A_1, C_1, $E_{\mathrm{peak},1}$, Eg_1, A_2, C_2, $E_{\mathrm{peak},2}$, and Eg_2. These fitting coefficients can be determined via fitting the ellipsometric parameters ψ and Δ based on regression analysis. The fitting process is carried out via the commercial analysis software. The corresponding figure of merit is shown as follows [21]:

$$MSE = \sqrt{\frac{1}{M-13-1}\sum_{k=1}^{M}\left(\left[\frac{\psi_{\mathrm{calc}}(E_k)-\psi_{\mathrm{meas}}(E_k)}{\delta\psi(E_k)}\right]^2 + \left[\frac{\Delta_{\mathrm{calc}}(E_k)-\Delta_{\mathrm{meas}}(E_k)}{\delta\Delta(E_k)}\right]^2\right)}, \tag{9}$$

where M is the number of measured points. $\delta\psi$ represents the measurement error of ψ, and $\delta\Delta$ represents the measurement error of Δ. E_k is the energy of the kth incident photon.

III. RESULTS AND ANALYSIS

The measured and calculated ellipsometric parameters of Cu films annealed at the temperature from 300 to 1200 K were well first investigated. Figures 1(a)–1(j) show the fitting results of ψ and Δ in the spectral of 0.73 to 6.42 eV at temperature from 300 to 900 K at the incident angle of 60°. The similar line shape of these ellipsometric parameters indicates that the annealing treating below 900 K does not cause the significant changes of optical properties of Cu films. Figures 1(k) and 1(l) show the fitting results of ψ and Δ in the spectral of 0.73 to 2.9 eV at temperature from 1000 to 1200 K at the incident angle of 60°, respectively. Obviously, the ellipsometric parameters above 900 K are significantly different from that below 900 K, which reflects the large difference between the annealing effects at high temperature and at low temperature. In order to clearly identify the annealing temperature effects, the fitting results of ψ and Δ as a function of annealing temperature at several representative photon energies are further given in Figs. 2(a) and 2(b), respectively. It can be seen that almost all the ψ and Δ curves show a clear "W-shaped" line shape with a central inflection point at 600 K. Notably, the variation trends of ψ and Δ are about 1–3° and 5–10°, respectively, which are much larger than the measurement precision and the random fluctuation of ψ and Δ reported by the spectroscopic ellipsometer [21]. Although the curves of ellipsometric parameters at 1 and 2 eV are relatively flat, a W-shaped line shape with the central inflection point at 600 K can still be observed. Additionally, the same feature can be observed at all the wavelength points if the entire spectrum is scanned, which indicates a possible transition of optical properties of annealed Cu films at 600 K when the annealing temperature increases from below 600 to above 600 K.

Then, the pseudodielectric functions were directly calculated from the measured ellipsometric parameters, which could be used to qualitatively evaluate the metallic or dielectric properties and the scattering properties of the samples. Figures 3(a) and 3(b) show the calculated pseudodielectric functions $\langle\varepsilon\rangle$ of Cu films annealed at 300, 500, 600, 800, 900, 1000, and 1200 K. Notably, each pseudodielectric function $\langle\varepsilon\rangle$ corresponding to the temperature in [300, 900 K] exhibits a Drude-like line shape in the low-photon energy range from 0.73 to 2.0 eV, and two absorption peaks due to the interband transitions in the high-photon energy range from 2.0 to 6.42 eV. These features are very similar to that exhibited by typical metals [31]. Correspondingly, the pseudodielectric function $\langle\varepsilon\rangle$ of Cu films annealed at temperature in [1000, 1200 K] exhibits a positive real part and absorption peak in the low-photon energy range from 0.73 to 3.0 eV. Such changes in the line shape of $\langle\varepsilon\rangle$ indicates that there is a transition from metallic properties to dielectric properties at 900 K. The dependency of $\langle\varepsilon\rangle$ on the incident angles was also presented in Figs. 3(c) and 3(d). It is obvious to see that $\langle\varepsilon\rangle$ becomes angle dependent above 900 K, indicating the existence of strong Mie-scattering property above 900 K.

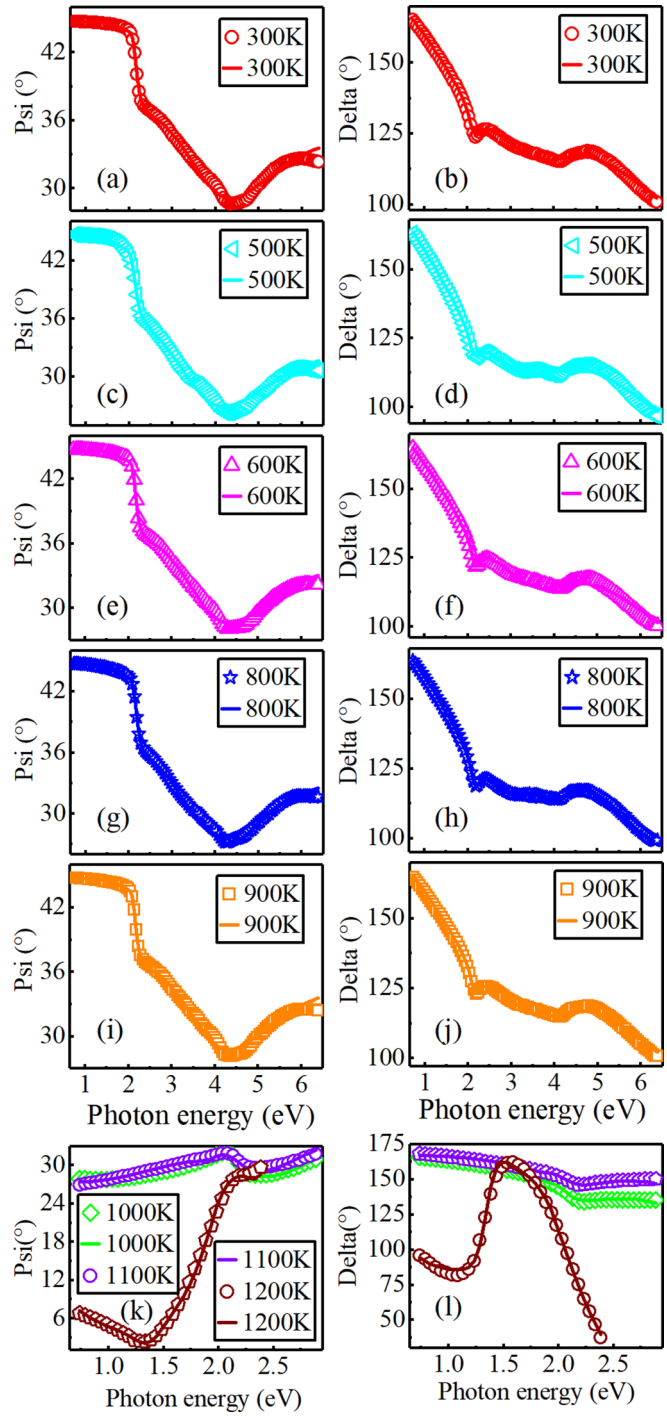

FIG. 1. Fitting results of ψ and Δ for Cu films annealed at temperature from 300 to 1200 K at the incident angle of 60°. (a), (b) Fitting results of ψ and Δ at temperature from 300 K, respectively. (c), (d) Fitting results of ψ and Δ at temperature from 500 K, respectively. (e), (f) Fitting results of ψ and Δ at temperature from 600 K, respectively. (g), (h) Fitting results of ψ and Δ at temperature from 800 K, respectively. (i), (j) Fitting results of ψ and Δ at temperature from 900 K, respectively. (k), (l) Fitting results of ψ and Δ at temperature from 1000 to 1200 K, respectively. Circles represent the measurement values, while solid lines stand for the calculated values.

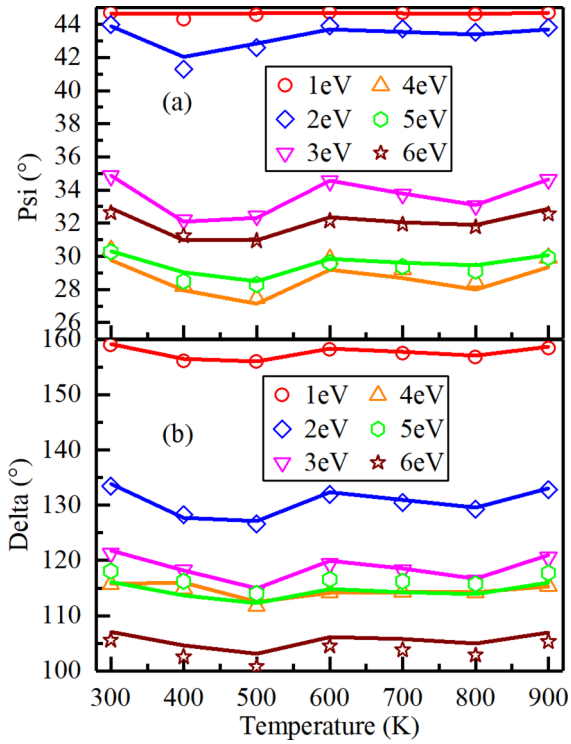

FIG. 2. Fitting results of ψ and Δ for Cu films annealed at temperature from 300 to 900 K at the incident angle of 60°. (a) Fitting results of ψ; (b) Fitting results of Δ. Circles represent the measurement values, while solid lines stand for the calculated values. Both ψ and Δ exhibit a transition temperature at 600 K, at which the variation tendency of both ψ and Δ will change.

Moreover, the generation of Mie-scattering property indicates a striking transition in the surface morphology of Cu films when the annealing temperature increases from below 900 K to above 900 K. Meanwhile, the depolarization, describing the degree of transforming from totally polarized incident light to partially polarized light during the ellipsometry, is used to estimate the surface scattering effect. The depolarization can be calculated from the Mueller matrix elements which were simultaneously measured by the ellipsometer. The corresponding equation is as follows:

$$Dep = \left[1 - \left(\frac{m_{12}+m_{21}}{-2m_{22}}\right)^2 - \left(\frac{m_{33}+m_{44}}{2m_{22}}\right)^2 - \left(\frac{m_{34}-m_{43}}{2m_{22}}\right)^2\right] \times 100\%, \quad (10)$$

where Dep is the depolarization. m_{12}, m_{21}, m_{22}, m_{33}, m_{34}, m_{43}, and m_{44} are the measured Mueller matrix elements.

It can be found that the depolarization increases from 5.0 to 10.0 at the incident angle of 60° with the increasing of annealing temperature, as shown in Fig. 4(a). The results indicate that there always exist small surface scattering due to the surface roughness of Cu films. Meanwhile, the dependency of depolarization on the incident angle was presented in Fig. 4(b). As the annealing temperature increases from below 900 K to above 900 K, the incident-angle dependency of depolarization becomes conspicuous, and the maximum

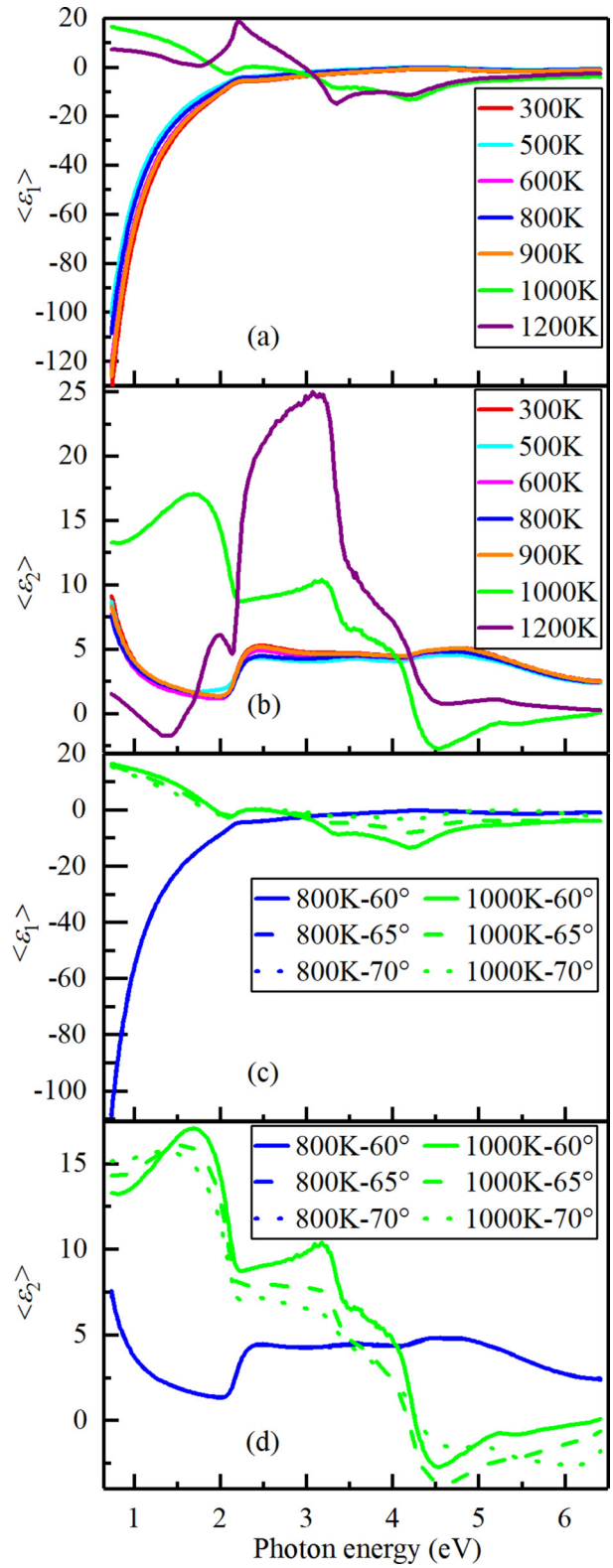

FIG. 3. Pseudodielectric functions $\langle\varepsilon\rangle$ of annealed Cu films. (a) The real part $\langle\varepsilon_1\rangle$ and (b) the imaginary part $\langle\varepsilon_2\rangle$ corresponds to 300, 500, 600, 800, 900, 1000, and 1200 K. (c) The real part $\langle\varepsilon_1\rangle$ and (d) the imaginary part $\langle\varepsilon_2\rangle$ of Cu films annealed at 800 and 1000 K at the incident angle of 60°, 65°, and 70°. At the annealing temperature below 900 K, the angle dependency of $\langle\varepsilon\rangle$ can be ignored, while the angle dependency of $\langle\varepsilon\rangle$ is very apparent for the annealing temperature above 900 K.

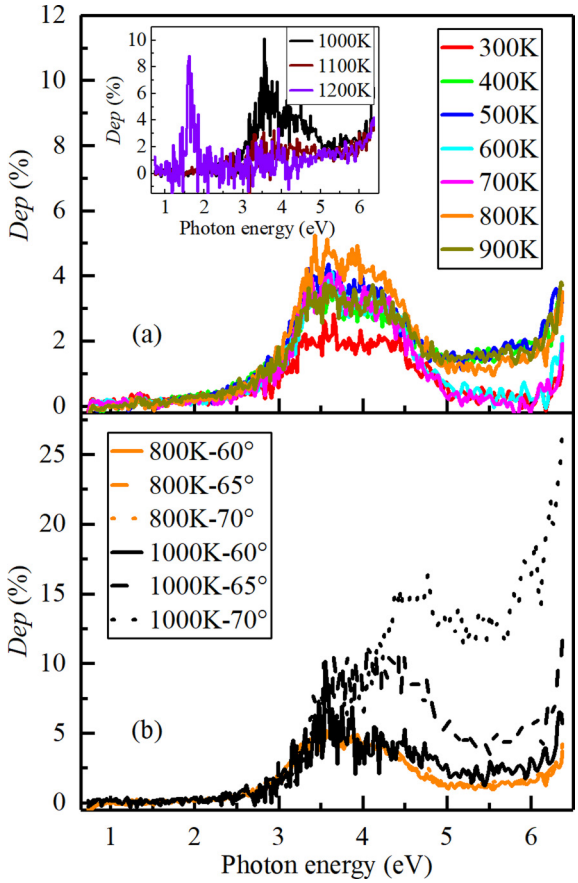

FIG. 4. Depolarization of annealed Cu films. (a) The temperature dependency of depolarization at incident angle of 60°. (b) The depolarization of Cu films annealed at 800 and 1000 K at the incident angle of 60°, 65°, and 70°. The depolarization of Cu films annealed at 1000, 1100, and 1200 K are shown in inset. At the annealing temperature below 900 K, the angle dependency of depolarization can be ignored, while the angle dependency of depolarization is very apparent for the annealing temperature above 900 K.

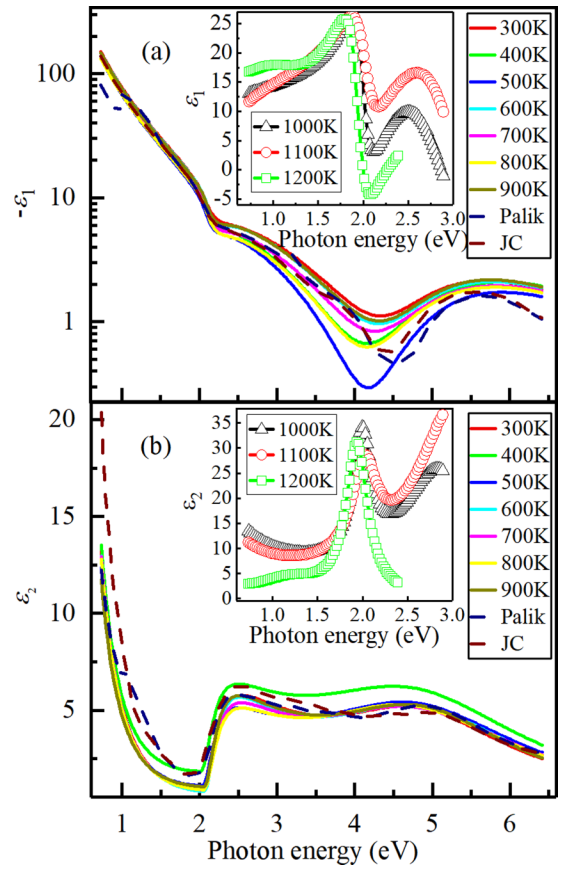

FIG. 5. Dielectric functions ε of Cu films annealed at different temperature from 300 to 1200 K. The dielectric functions are calculated from ellipsometric parameters via Drude-Tauc-Lorentz analysis. The real parts of ε corresponding to temperature from 300 to 900 K are displayed in a logarithmic fashion. The dielectric functions ε of Cu films annealed at 1000, 1100, and 1200 K are shown in insets. Dielectric functions of bulk Cu at 300 K reported by Palik [31] (dark blue dashed line) and John and Christy [32] (dark red dashed line) are shown for comparison. At the annealing temperature below 900 K, the dielectric functions of each annealed Cu film have great similarity with the published data. Both of them show prominent metallicity. However, at the annealing temperature above 900 K, the plasmonic feature is predominant in the dielectric functions.

depolarization reaches nearly 27 at the incident angle of 70°. These results also explain the existence of strong scattering property at the annealing temperature larger than 900 K.

Next, the Drude-Tauc-Lorentz analysis was carried out in the whole spectral range covering 0.73 to 6.42 eV, when the annealing temperature was less than 900 K. However, for the annealing temperature larger than 900 K, the Drude-Tauc-Lorentz analysis with two Lorentz terms was only carried out in the spectral range between 0.73 and 2.9 eV where the depolarization and the Mie-scattering effect are not significant, in order to reduce the fitting errors. The obtained dielectric functions of Cu films are shown in Fig. 5. The dielectric functions of Cu films annealed at temperature from 300 to 900 K are highly similar to the published data [31,32], indicating the conspicuous metallicity. The real part ε_1 in the photon energy range from 0.73 to 2.0 eV have changed from negative values to positive values at nearly 900 K. Moreover, two oscillating peaks gradually appear in ε_1 in the range of 1.5 to 2.0 eV when the annealing temperature increases above 900 K. As for the imaginary part ε_2, its steep absorption edge near 2.0 eV disappears, and is replaced by a sharp absorption peak with narrow broadening, when the annealing temperature increases from below 900 K to above 900 K. We can see that the plasmonic feature occurs and becomes predominant in the optical response at the annealing temperature above 900 K, which might be caused by the islands and hillocks formed on Cu films [33]. Besides, a blueshift of the plasmonic peak in the ε_2 has been noticed with the temperature increasing from 1000 to 1100 K, which might be attributed to the development of islands and the increasing in the discontinuity of Cu films [7]. As the temperature further increases from 1100 to 1200 K, a redshift of the plasmonic peak in the ε_2 has occurred, which might be due to the decrease of spacing between islands.

Along with the ellipsometry, the evolution of surface morphology and roughness of Cu films with different annealed temperature was investigated by AFM and WLI. The AFM images for the local surface morphology are shown in Fig. 6.

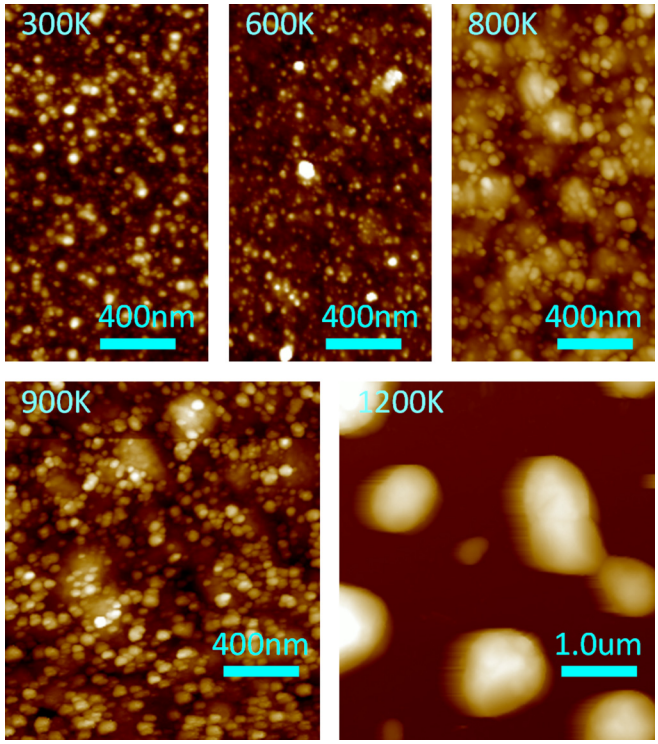

FIG. 6. Surface morphology of Cu films annealed at 300, 600, 800, 900, and 1200 K reported by AFM. All the micrographs are shown at the same scale of 500 nm. With the annealing temperature increasing, the Cu particles coalesce gradually to larger clusters. At the annealing temperature above 900 K, the islands or hillock are formed and separated.

We can see the particle size increases gradually from nearly 54 to 1470 nm and becomes an isolated and discontinuous morphology as the annealing temperature increases from 300 to 1200 K, due to the coalescence of the Cu particles. Correspondingly, the plasmonic feature becomes increasingly prominent when the annealing temperature is above 900 K as shown by the dielectric function in Fig. 5. For a more comprehensive analysis about the evolution of surface morphology, the surface roughness data of the Cu films annealed at the different temperature reported by ellipsometer, AFM, and WLI are listed in Table I. We can see all the roughness obtained from ellipsometer, AFM, and WLI exhibits two steep transitions at 600 and 900 K. Due to the different roughness metrology standards obeyed by AFM and WLI and the different size of measurement spot, the results reported by AFM highlight the locality of the morphology evolution with increasing annealing temperature, while the results reported by WLI emphasize the wholeness of the morphology evolution. When the annealing temperature is below 900 K, the morphology of samples remains as a continuous film. Therefore, the roughness reported by ellipsometry highlights the wholeness, and accordingly the evolution trend of surface morphology is consistent with that reported by WLI. When the annealing temperature is above 900 K, the morphology of sample is gradually transformed into an isolated island structure. Meanwhile, the ellipsometric measurement results are significantly affected by the scattering effect of the island structure. Due to the random distribution of islandlike particles, the scattering characteristics of Cu samples are similar to that of a single isolated island [34]. Correspondingly, the roughness reported by ellipsometry highlights the locality, and the evolution trend of surface morphology is consistent with that reported by AFM.

TABLE I. The surface roughness of annealed Cu films reported by ellipsometer, AFM, and WLI. T_a is the annealing temperature. d_s, R_a, S_{a1}, and S_{a2} represent measured values reported by ellipsometry with spot of 2 mm × 2 mm, AFM with spot of 5 um × 5 um, WLI with spot of 173.6 um × 173.6 um, and WLI with spot of 868.2 um × 868.2 um, respectively.

T_a (K)	300	400	500	600	700
d_s (nm)	3.13	4.92	3.71	2.32	2.24
R_a (nm)	0.60	0.45	0.51	3.51	5.84
S_{a1} (nm)	0.91	0.48	0.77	0.41	0.43
S_{a2} (nm)	1.70	1.43	1.88	1.70	1.89
T_a	800	900	1000	1100	1200
d_s (nm)	2.51	1.71	(57.48)	(54.9)	(113.2)
R_a (nm)	6.45	6.12	9.38	86.49	149.80
S_{a1} (nm)	0.88	0.92	2.25	7.38	2.51
S_{a2} (nm)	1.52	1.48	3.76	5.09	2.45

IV. DISCUSSION

A. Crystallite structure properties

XRD measurement was carried out to investigate the evolution of crystal structure and grain size of the annealed Cu films. As shown in Fig. 7, the as-deposited polycrystalline Cu film has three crystallites orientation along the (111), (200), and (220) directions at 300 K but only the (111) diffraction peak is predominant. The diffraction peaks corresponding to the copper silicide are not found in the pattern, which might be caused by the limitation of instrument and the weak block

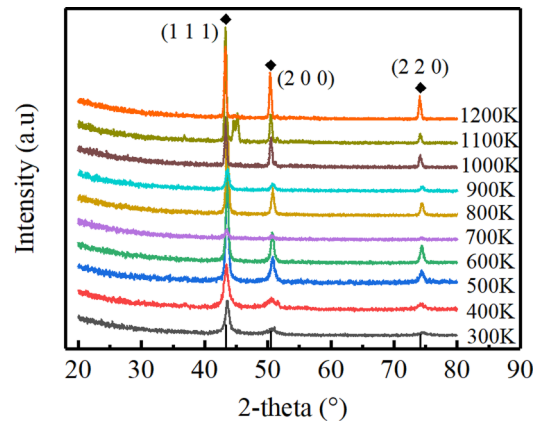

FIG. 7. X-ray diffraction pattern of Cu films annealed at different temperature from 300 to 1200 K. All the diffraction patterns have three diffraction peaks at 43.4°, 50.5°, and 74.2°, corresponding to (111), (200), and (220) of Cu (ICSD-53247). With the annealing temperature increasing, both the 111, 200, and 220 peaks have exhibited obvious dynamic changes, which indicate the evolution of crystal structures in the Cu films.

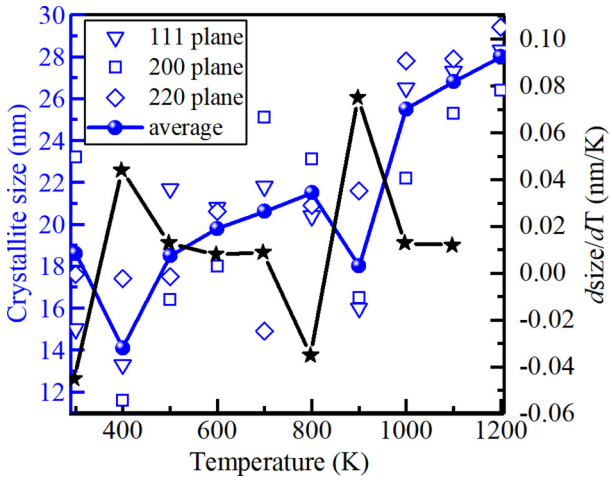

FIG. 8. The crystallite sizes in the (111), (200), and (220) plane obtained by XRD, the average crystallite size, and the thermal differential of average size. With the annealing temperature increasing from 300 to 1200 K, all the crystallite sizes exhibit the gradual upward trends.

effect of a native oxide at the interface between the Cu layer and Si (100) substrate [33]. The native oxide can hinder the diffusion of Cu atoms or Si atoms across the interface. As the annealing temperature increases gradually from 300 to 600 K, all the three peaks along the (111), (200), and (220) directions become sharper and more obvious, indicating more crystallization of Cu grains in the film. The predominant peak along the (111) direction reflects the preferential orientation of Cu crystallites, the enhanced diffusion of Cu particles, and the more unstable thermodynamics properties [35]. At the annealing temperature of 700 and 900 K, all the diffraction peaks become much weaker, which indicates the reducing crystallinity of Cu films. While at the annealing temperature at 800 K, which is in between 700 and 900 K, the diffraction pattern is similar to that at 600 K, presenting the similar good crystallinity. These XRD patterns at temperature from 600 to 900 K show that the crystalline state in the Cu films is fluctuating due to the thermal diffusion and the agglomeration of the (111)-oriented Cu crystallite. With the annealing temperature increasing further from 900 to 1200 K, the three diffraction peaks become evident with the weak sidelobes emerging, indicating the formation of islands.

Further, the crystallite size was calculated based on the Debye-Scherrer formula [36],

$$D = \frac{0.9\lambda}{\mathrm{FWHM}\cos\theta}, \tag{11}$$

where D is the crystallite size of each crystal plane. λ is the wavelength of Cu-$k_{\alpha 1}$ x ray, whose value is 0.154 nm. θ is the Bragg diffraction angle, and the FWHM is the full width at half maximum of each diffraction peak.

The dependence of the calculated crystallite size on the annealing temperature is shown in Fig. 8. We can see the crystallite sizes in the (111), (200), and (220) plane shows an increasing tendency as the increasing of annealing temperature, which is in agreement with the coalescing surface morphology presented in Fig. 6. Correspondingly, the average crystallite size exhibits a continual trend of increasing except the two anomalous points at 400 and 900 K. Then the linear function $D = D_0 + cT$ was used in the temperature range [500, 800 K] and [1000, 1200 K] to fit the average crystallite sizes. The increasing coefficients c was 0.0096 and 0.0127 nm/K, respectively. The results indicate the raised growth rate of Cu crystallites, which further reflects the increased aggregation velocity and migration rate of Cu particles due to the increasing of annealing temperature. Meanwhile, the growth processes of Cu clusters should be divided into two main stages, in which both the driving force and the activation energy might be altered in a complicated way by the structure change due to high annealing temperature. In the first stage corresponding to [500, 800 K], the Cu clusters with crystallite size slightly larger than that of pristine Cu film at 300 K gradually form inside the film due to the diffusion of particles along the grain boundary. Therefore, the surface roughness slightly decreases due to the flattening of Cu films, according to the results by ellipsometry as shown in Table I. Moreover, the strain produced by the mismatch between Cu, SiO_2 interlayer, and Si has been relaxed by the annealing process, which might be responsible for the cluster formation. In the second stage corresponding to [1000, 1200 K], the continuous Cu films fade out and the isolated Cu islands gradually form due to the aggregation of Cu clusters. Further, the numerical differential of average crystallite size with respect to the annealing temperature was calculated and shown in Fig. 8. Two local maximum inflection points at 400 and 900 K are noticeable, and the two temperature points have split the evolution process into two main stages. The activation energy corresponding to grain-boundary migration in the two stages can be calculated via fitting the differential with the empirical equation [37,38],

$$G = G_0 \exp\left(\frac{-Q}{k_B T}\right), \tag{12}$$

where G_0 and Q are the rate constant and the activation energy, respectively. T stands for the absolute temperature, and $k_B = 1.3806 \times 10^{-23}$ J/K is the Boltzmann constant.

Correspondingly, the activation energies for grain-boundary migration in the two main stages are calculated as 0.179 and 1.142 eV, respectively. The former energy is rather close to that of Au deposited on SiO_2 [33], which indicates that the main forming mechanism of clusters inside Cu films is the grain-boundary migration. The latter explains that there exist other dominant mechanisms besides the migration of Cu particles along the grain boundary, such as the coalescence of clusters on the film surface and the destruction of continuous films.

Further, the average lattice parameters of the annealed Cu, belonging to the faced-centered cubic structure, were also determined from the XRD patterns based on the Rietveld procedure. The corresponding results are shown in Fig. 9. At the same time, both the calculated lattice parameters of Cu under different heating temperature and annealing temperature obtained from molecular-dynamics simulations are also shown in Fig. 9. It can be noticed that the measured lattice parameters exhibit an increasing tendency with an anomalous segment at 900 K as the annealing temperature increases progressively. By contrast, the lattice parameters reported by

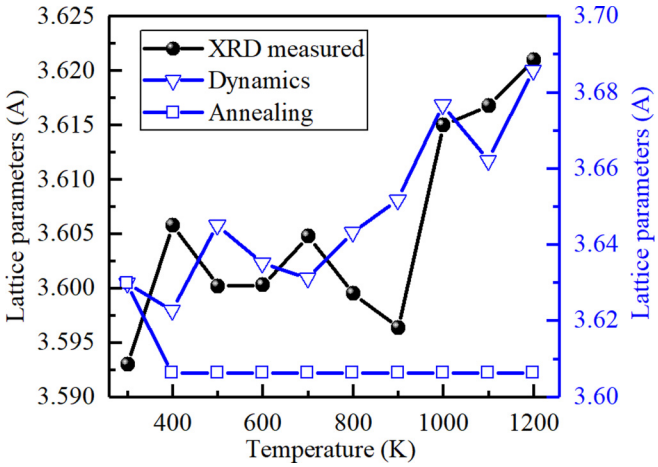

FIG. 9. The average lattice parameters obtained by XRD, thermal dynamics simulations, and annealing dynamics simulations. Both the thermal dynamics simulations and annealing dynamics simulations are carried out based on molecular dynamics.

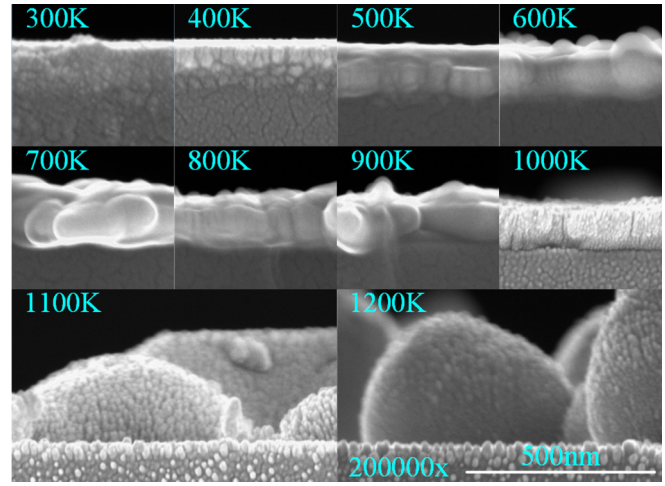

FIG. 10. Sectional view of Cu films annealed at different temperature. All the images are presented at the same scale and magnification. With increasing the annealing temperature, the Cu particles reaggregate on the lateral scale and eventually form island structure.

the heating dynamics simulations increase markedly from 3.63 to 3.69 Å, which is roughly in accordance with the linear thermal expansion. As for the lattice parameters reported by the annealing dynamics simulations, they only exhibit a decrease from 3.63 to 3.605 Å at [300, 500 K] and remain nearly constant across from 500 to 1200 K. The results mainly reflect the cooling relaxation of lattice at different temperatures, which are responsible for the discrepancy between the measured and calculated lattice parameters. The differences between the measured lattices parameters and the heating dynamics results explain that the actual annealing effects are a trade-off between the heating expansion and the cooling relaxation.

B. Morphology evolution

The agglomeration of crystallites and the evolution of clusters with respect to annealing temperature were investigated by SEM. The corresponding sectional views are shown in Fig. 10. The crystallites in the raw polycrystalline are randomly orientated and its shape is almost spherical, which indicates the partial crystallization in the Cu films during the deposition. When the annealing temperature increases to 400 and 500 K, the conspicuous columnar grains are formed and densely arranged on the top of the Cu layer. Due to the elimination of internal stress caused by the growth process, the grain arrangement state changes from multiple short-range orders to the overall long-range orders. These results indicate that the temperature rise of 100 K greatly drives the migration and the recrystallization of Cu nanoparticles. As the annealing temperature increases to [600, 900 K], the grains begin to grow laterally remarkably, and the twin lamellas are formed in some localized region [39]. In this stage, Cu nanoparticles migrate mainly along the lateral grain boundaries, and all the migrations are always carried out inside the film layer, which corresponds to the rather small activation energy calculated previously. With the annealing temperature reaching [1000, 1200 K], the continuous Cu film is transformed into many isolated islands due to the longitudinal migration of Cu nanoparticles, which corresponds to the slightly larger activation energy calculated previously. It is worth noting that for the Cu films annealed at 1100 and 1200 K, a close-packed refined grain layer with consistent orientation and uniform size appears between the isolated island structure and the Si substrate.

C. Annealing-temperature dependent dielectric properties

As shown in Fig. 5, the dielectric functions of the original Cu film are slightly different from that measured by Palik and Johnson and Christy [31,32], which can be attributed to the different preparation procedures and sample types [40,41]. However, the dc resistivity $\rho_{dc} = 1.80\,\mu\Omega\,\text{cm}$ and the electron scattering time $\tau = 18.475$ fs of Cu film at room temperature are in good consistency with that of bulk Cu [42]. Figure 11 shows the dependence of dc resistivity ρ_{dc} obtained from the fitting procedures and the layer resistivity ρ_{layer} calculated from the measured sheet resistance R_{sheet} with the equation

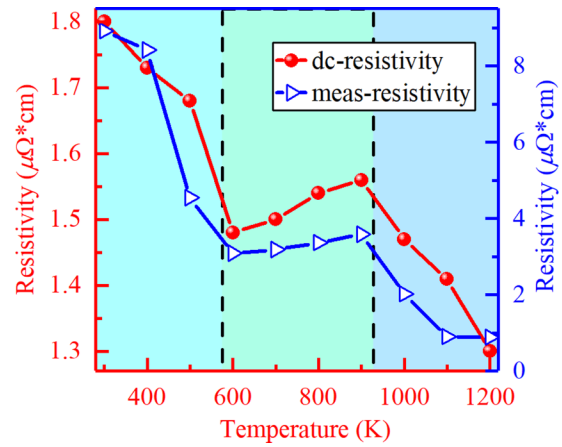

FIG. 11. dc resistivity obtained from fitting procedures and layer resistivity measured via four-probe method.

$\rho_{layer} = R_{sheet} d_{Cu}$ on the annealing temperature. Both the dc resistivity ρ_{dc} and the layer resistivity ρ_{layer} exhibit a highly similar decrease tendency with the increasing of annealing temperature. Moreover, two transition points can be found in both ρ_{dc} and ρ_{layer} at 600 and 900 K. In fact, the decrease tendency might be attributed to the effect of grain-boundary scattering according to the Mayadas-Shatzkes theory [44]. With the increasing of annealing temperature, the average crystallite size D increases from 14 to 28 nm as shown in Fig. 8, which is always less than the mean-free path $L =$ 40 nm for noble metal [43]. After using the coefficient of reflection $R = 0.24$ at the grain boundary for Cu [44], the structural parameter α can be evaluated based on the equation $\alpha = LR/[D(1 - R)]$. Notably, the structural parameter α is always less than 1, and decreases with the average crystallite size. Since the film resistivity is the monotonically increasing function of the structural parameter α, the film resistivity decreases with the increasing of the annealing temperature. Meanwhile, the temperature coefficient of dc resistivity (TCR $= \rho^{-1}\partial\rho/\partial T$) was numerically calculated [45]; it also reflects two transition points at 600 and 900 K. When the annealing temperature is below 600 K, TCR always remains negative and decreases from -0.0193 to $-0.2029\,K^{-1}$ with increasing temperature, and then the TCR turns into positive values about $1.818 \times 10^{-2}\,K^{-1}$ when the annealing temperature increases to values between 600 and 900 K. When the annealing temperature keeps increasing above 900 K, the TCR turns into negative values, which is around $-6.028 \times 10^{-2}\,K^{-1}$. As for the variation tendency of TCR changes at 600 K, it can be attributed to the disappearance of disorder caused by thermally excited phonons [46]. Meanwhile, it is worth noting that the dc resistivity increases from 1.48 to 1.56 $\mu\Omega$ cm as the annealing temperature increasing from 600 to 900 K, nearly following the linear temperature dependency, which might be due to the increasing electron-phonon scattering [47]. At the annealing temperature above 900 K, it is anomalous to observe the further decreasing tendency of dc resistivity, since the transformation of morphology from a continuous film into an isolated island structure usually makes the sample dielectric. However, it can be noticed that as shown in Fig. 10, a close-packed refined nanoparticle layer with consistent orientation and uniform size has been formed between the Cu islands structure and the Si substrate, which results in the excellent conductive property of the Cu film annealed at temperature above 900 K. Although the diffraction peak corresponding to the Cu-Si compound was not observed in the XRD spectral, we can still speculate that the composition of the nanoparticle layer might be copper silicide [48]. Since the thickness of native oxide on the original Si substrate is solely 1.89 nm, it may be difficult to block the thermal diffusion of Cu atoms toward Si substrate [49]. Meanwhile, the annealing at high temperature larger than 900 K can cause the formation of self-assembled copper-silicide nanowires or nanoislands [49,50]. These copper-silicide nanoparticles with consistent orientation, uniform size, and dense alignment in the annealed Cu films would contribute to the surprisingly excellent conductivity. In order to confirm the assertion, another set of samples consisting of 100-nm-thick Cu film above the 600-nm-thick SiO_2 covered on the Si substrate have been prepared and then annealed at temperature from 1000 and

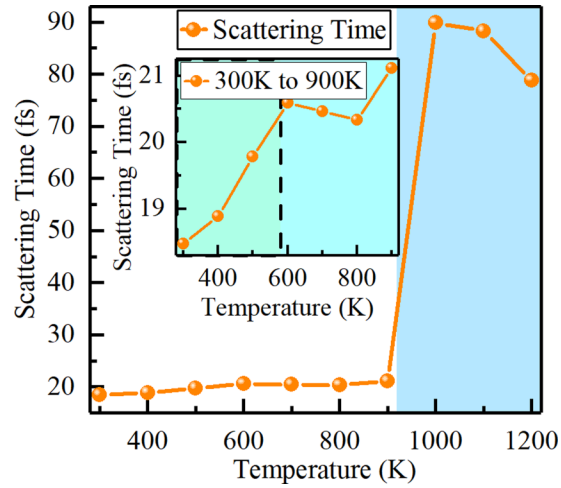

FIG. 12. Scattering time of conduction electrons at each annealed Cu film.

1200 K. The SiO_2 layer is sufficiently thick to block the thermal diffusion of Cu atoms towards the Si substrate and the formation of metallic copper-silicide [51]. The results of the dc resistivity measurement via four-probe method indicate that all the supplementary samples are insulators after the annealing. Meanwhile, the cross-section view of these samples reported by SEM shows that although a similar Cu island structure has been formed on the SiO_2 layer, the underneath-formed nanoparticles are disorderly oriented and sparsely arranged, which leads to the insulation of the supplementary samples.

Besides, due to the large Cu islands with vertical height of 456.03 ± 107.5 nm in the original sample, both the scattering property and the plasmon property are dominant in the dielectric functions, while the Drude-like feature caused by the annealed Cu islands and the underneath metallic nanoparticles layer might be minor and inconspicuous. However, the dc resistivity in the Drude term still indicates the excellent electrical property, as shown in Fig. 11. In contrast, the ellipsometric parameters of the supplementary samples are much more severely affected by the scattering effects of Cu islands, making it difficult to be analyzed with the Drude model, which indicates the insulating property of the supplementary sample.

The scattering time of conduction electrons for Cu films obtained from the fitting procedure is shown in Fig. 12. The scattering time increases from 21 fs below 900 K to 89 fs at 900 K due to the formation of isolated islands, indicating the transition temperature is at 900 K. It can be seen from the inset of Fig. 12 that the relaxation time increases from 18 fs at 300 K to 20.5 fs at 600 K, showing another probable transition point at 600 K. The increasing tendency is similar to the measured temperature-dependent Drude broadening of Ag films [52], which indicates that the dominant effect is the weakening interaction between electrons and phonons. However, the discrepancy in the evolution of relaxation time between the annealed Cu films and the heated Ag films is somewhat noticeable, which can be attributed to the cooling relaxation of lattice at each annealing temperature as shown in Fig. 9. A possible saturation of the scattering time at 600 K can be observed, which is different from the saturation

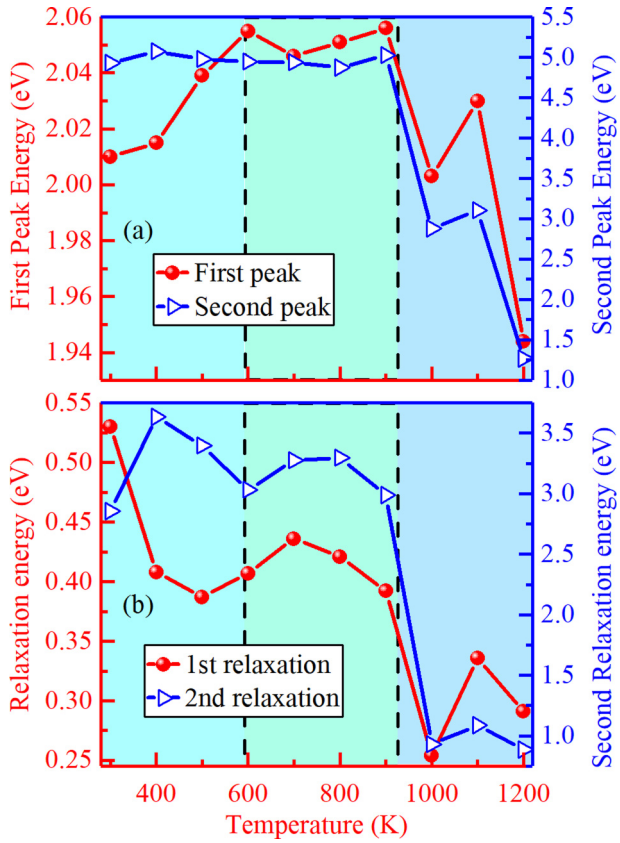

FIG. 13. Absorption peak energy and relaxation time of conduction electrons at each annealed Cu film.

of scattering rate reported in the literature [47]. Since the scattering rate is inversely related to the scattering time, when the scattering rate increases to a saturation value, the scattering time would be expected to show decreasing to a saturation value, which is opposite to what was reported in our paper. The reason for the discrepancy is because they are two different processes. Comparing with the general *in situ* temperature loading, the annealing process has one more step, which is the cooling-relaxation process. This process would cause the relaxation of thermal effects, which will make the Cu films in an equilibrium state rather than a thermally excited state. This is why our analysis results, such as scattering time and dc resistivity, are significantly different from that reported in literature [46,47,52,53].Consequently, the Mott-Ioffe-Regel limit of metallic transport marked by the saturation of scattering rate was not observed in our experiments [47]. Additionally, as the scattering time reaches a possible saturation value at 600 K, the variation tendency of dc-resistivity changes from a clifflike decline to a slight increase, which directly violates the criterion for the Mott-Ioffe-Regel limit [46].

Both the absorption-peak energy and the relaxation energy of the first and second interband transitions are shown in Fig. 13. Both the first absorption-peak energy curve and the two relaxation energy curves exhibit a three-stage evolution, in which two transition points at 600 and 900 K can be observed. When the annealing temperature is below 600 K, the first absorption-peak energy shifts from 2.01 to 2.055 eV, all of which are in good agreement with the literature [31,32,40], while the first absorption peak energy remains near 2.05 eV with the fluctuation less than 0.2%, as the annealing temperature is in the range of 600 to 900 K. With the annealing temperature above 900 K, the first absorption-peak energy exhibits a decreasing tendency with a significant oscillation, which can be attributed to the earlier discussed evolution of plasmon peak due to island development. As for the second absorption-peak energy, it is almost unaffected by the temperature and maintains near 4.95 eV corresponding to the band 6 $\rightarrow$ band 7 transition [54], with annealing temperature below 900 K. When annealing temperature is higher than 900 K, the second absorption-peak energy decreases to less than 2.9 eV, which indicates a possible additional plasmon peak. Further, both the first and second relaxation energy exhibit the decreasing tendency when the annealing temperature is below 600 K, while they remain stable values when the annealing temperature is in the interval from 600 to 900 K. When the annealing temperature is beyond 900 K, with the formation of island structure, both the first and second relaxation energy show an obvious oscillation. In comparison with the reported *in situ* heating experiment [19,54,55], the above results show a significant discrepancy, which is because the sample has been sufficiently relaxed and reaches a possible equilibrium state during the cooling step in the annealing process. In summary, two possible transition points of the optical properties with respect to annealing temperature, which are 600 and 900 K, respectively, are observed. The transition at 600 K mainly refers to the transition of crystalline state incubated inside the Cu film, while the transition at 900 K refers to the morphological transition of Cu sample from a continuous film to an island structure.

V. CONCLUSION

In summary, the dielectric functions, the morphology, and the structural properties evolutions of Cu films with nominal thickness of 100 nm annealed at different temperature from 300 to 1200 K have been studied thoroughly. Spectroscopic ellipsometry in the spectral range of 0.73 to 6.42 eV has been employed to determine the dielectric functions of the annealed Cu films. The annealing-temperature dependent parameters such as the dc resistivity, the electron relaxation time, the absorption peaks, and the broadening parameters have been analyzed based on the dielectric function and the Drude-Tauc-Lorentz-IR pole analysis. Two transition points at around 600 and 900 K have been observed. At the former transition temperature, the dc resistivity reduces from $1.8 \times 10^{-6}\,\Omega\,\mathrm{cm}$ to $1.5 \times 10^{-6}\,\Omega\,\mathrm{cm}$, the corresponding temperature coefficient of dc resistivity changes from $-0.2029\,\mathrm{K}^{-1}$ to $1.818 \times 10^{-2}\,\mathrm{K}^{-1}$, the electron scattering time increases from 18 fs to a saturation value of 20.5 fs, the first absorptive-peak energy rises from 2.01 to 2.055 eV, and the corresponding temperature-dependency coefficient transforms from $1.5 \times 10^{-4}\,\mathrm{eV/K}$ to nearly 0 eV/K. At the latter one, the dc resistivity reduces from $1.56 \times 10^{-6}\,\Omega\,\mathrm{cm}$ to $1.30 \times 10^{-6}\,\Omega\,\mathrm{cm}$ again, the corresponding temperature coefficient of dc resistivity changes from $1.818 \times 10^{-2}\,\mathrm{K}^{-1}$ to $-6.028 \times 10^{-2}\,\mathrm{K}^{-1}$, the electron relaxation time sharply increases from 21 to 89 fs, and the plasmon properties become notable at nearly 2.0 eV. The evolution of dc resistivity with

annealing temperature has also been verified by the results achieved using four-probe method, and the evolution mechanism can be attributed to the scattering effect at the grain boundary and disappearance of disorder caused by thermally excited phonons. The dependence of these electronics parameters on annealing temperature has been compared with the temperature-dependent parameters of Ag films and rare-earth-doped $CaFe_2As_2$, the discrepancies of which highlight the relaxation effects due to the cooling procedure in the annealing. Meanwhile, WLI, AFM, and SEM have been used to characterize the surface and cross-section topography to study the evolution of morphology changes induced by different annealing temperature, whose results would be used as the prior knowledge for the reasonable construction of optical model in the ellipsometry analysis. XRD experiments have been carried out to determine the evolutionary structural properties of Cu films. The evolutions of crystallite sizes and lattice parameters have been calculated according to the Debye-Scherrer formula and Rietveld procedure, which indicates the two transition points of 400 and 900 K. Correspondingly, the activation energies for grain-boundary migration in the two main stages are calculated as 0.179 and 1.142 eV, respectively

ACKNOWLEDGMENTS

The National Natural Science Foundation of China (Grants No. 51575214, No. 51525502, No. 51975232, and No. 51727809); the National Key Research and Development Plan funded this work (Grant No. 2017YFF0204705); the Natural Science Foundation of Hubei Province of China (Grant No. 2018CFA057); and the National Science and Technology Major Project of China (Grant No. 2017ZX02101006-004). We would like to thank Ms. Yan Zhu and Mr. Jianlin Chu for SEM and WLI measurements in Micro and Nano Fabrication and Measurement Laboratory of Collaborative Innovation Center for Digital Intelligent Manufacturing Technology and Application. The authors also thank Mr. Zhekun Chen for AFM measurements in School of Artificial Intelligence and Automation, HUST.

[1] Y. K. Mishra, S. Mohapatra, R. Singhal, and D. K. Avasthi, Appl. Phys. Lett. **92**, 043107 (2008).
[2] A. Dualeh, N. Tétreault, T. Moehl, P. Gao, M. K. Nazeeruddin, and M. Grätzel, Adv. Funct. Mater. **24**, 3250 (2014).
[3] Y. Hu, R. Sharangpani, and S. Tay, J. Vac. Sci. Technol. A **18**, 2527 (2000).
[4] B. Kuerbanjiang, C. Love, D. Kepaptsoglou, Z. Nedelkoski, S. Yamada, A. Ghasemi, Q. M. Ramasse, and K. Hamaya, J. Alloys Compd. **748**, 323 (2018).
[5] T. Itoh, M. Mori, M. Inukai, H. Nitani, T. Yamamoto, T. Miyanaga, N. Igawa, N. Kitamura, N. Ishida, and Y. Idemoto, J. Phys. Chem. C **119**, 8447 (2015).
[6] S. Nakashima, K. Fujita, K. Tanaka, K. Hirao, T. Yamamoto, and I. Tanaka, J. Magn. Magn. Mater. **310**, 2543 (2007).
[7] Š. Meškinis, A. Ciegis, A. Vasiliauskas, K. Šlapikas, R. Gudaitis, I. Yaremchuk, V. Fitio, Y. Bobitski, and S. Tamulevicius, Nanoscale Res. Lett. **11**, 146 (2016).
[8] S. D'Elia, N. Scaramuzza, F. Ciuchi, C. Versace, G. Strangi, and R. Bartolino, Appl. Surf. Sci. **255**, 7203 (2009).
[9] X. D. Li, T. P. Chen, Y. Liu, and K. C. Leong, Opt. Express **22**, 23086 (2014).
[10] Kh. A. Abdullin, G. Cicero, L. V. Gritsenko, S. E. Kumekov, and A. A. Markhabaeva, J. Appl. Phys. **121**, 245303 (2017).
[11] M. Hövel, B. Gompf, and M. Dressel, Phys. Rev. B **81**, 035402 (2010).
[12] G. Bao, D. Duan, F. Tian, L. Wang, B. Liu, and T. Cui, J. Chem. Phys. **134**, 034508 (2011).
[13] J. Zhang, S. Zhang, H. Weng, W. Zhang, L. Yang, Q. Liu, S. Feng, X. Wang, R. Yu, L. Cao, L. Wang, W. Yang, H. Liu, W. Zhao, S. Zhang, X. Dai, Z. Fang, and C. Jin, Proc. Natl. Acad. Sci. USA **108**, 24 (2011).
[14] A. Masten and P. Wissmann, Appl. Surf. Sci. **179**, 68 (2001).
[15] H. U. Yang, J. D'Archangel, M. L. Sundheimer, E. Tucker, G. D. Boreman, and M. B. Raschke, Phys. Rev. B **91**, 235137 (2015).
[16] J. M. E. Harper and K. P. Rodbell, J. Vac. Sci. Technol. B **15**, 763 (1997).
[17] G. H. Chan, J. Zhao, E. M. Hicks, G. C. Schatz, and R. P. V. Duyne, Nano Lett. **7**, 1947 (2007).
[18] A. Naldoni, F. Riboni, U. Guler, A. Boltasseva, V. M. Shalaev, and A. V. Kildishev, Nanophotonics. **5**, 112 (2016).
[19] M. Xu, J.-Y. Yang, S. Zhang, and L. Liu, Phys. Rev. B **96**, 115154 (2017).
[20] J. Liu, J. Lin, H. Jiang, H. Gu, X. Chen, C. Zhang, G. Liao, and S. Liu, Phys. Scr. **94**, 085802 (2019).
[21] H. Fujiware, *Spectroscopic Ellipsometry Principles and Applications* (Wiley, New York, 2007).
[22] R. L. Olmon, B. Slovick, T. W. Johnson, D. Shelton, S.-h. Oh, G. D. Boreman, and M. B. Raschke, Phys. Rev. B **86**, 235147 (2012).
[23] R. A. Synowicki, C. M. Herzinger, J. T. Hall, and A. Malingowski, Appl. Surf. Sci. **421**, 824 (2017).
[24] T. E. Tiwald, D. W. Thompson, J. A. Woollam, W. Paulson, and R. Hance, Thin Solid Films **313–314**, 661 (1998).
[25] G. E. Jellison, Jr. and F. A. Modine, Appl. Phys. Lett. **69**, 371 (1996).
[26] G. E. Jellison, Jr. and F. A. Modine, Appl. Phys. Lett. **69**, 2137 (1996).
[27] H. G. Tompkins and E. A. Irene, *Handbook of Ellipsometry* (William Andrew Publishing, New York, 2004).
[28] D. E. Aspnes, Thin Solid Films **89**, 249 (1982).
[29] D. E. Aspnes, Phys. Rev. B **25**, 1358 (1982).
[30] S. De Zuani, M. Rommel, B. Gompf, A. Berrier, J. Weis, and M. Dressel, ACS Photonics **3**, 1109 (2016).
[31] E. D. Palik, *Handbook of Optical Constants of Solid* (Academic, San Diego, 1998).
[32] P. B. Johnson and R. W. Christy, Phys. Rev. B **6**, 4370 (1972).
[33] V. L. D. L. Santos, D. Lee, J. Seo, F. L. Leon, D. A. Bustamante, S. Suzuki, Y. Majima, T. Mitrelias, A. Ionescu, and C. H. W. Barnes, Surf. Sci. **603**, 2978 (2009).

[34] S. De Zuani, M. Rommel, R. Vogelgesang, J. Weis, B. Gompf, M. Dressel, and A. Berrier, Plasmonics **12**, 1381 (2017).
[35] V. Švorčík, O. Kvítek, O. Lyutakov, and J. Siegel, Appl. Phys. A **102**, 747 (2011).
[36] G. Yang, X. Fu, and J. Zhou, J. Opt. Soc. Am. B **30**, 282 (2013).
[37] L. L. Levenson, Appl. Phys. Lett. **55**, 2617 (1989).
[38] N. Mancini and E. Rimini, Surf. Sci. **22**, 357 (1970).
[39] L. Lu, Y. Shen, X. Chen, L. Qian, and K. Lu, Science **304**, 422 (2004).
[40] K. Stahrenberg, Th. Herrmann, K. Wilmers, N. Esser, W. Richter, and M. J. G. Lee, Phys. Rev. B **64**, 115111 (2001).
[41] J. Trollmann and A. Pucci, J. Phys. Chem. C **118**, 15011 (2014).
[42] H. Ehrenreich and H. R. Philipp, Phys. Rev. **128**, 1622 (1962).
[43] E. Hu, Q. Cai, R. Zhang, Y. Wei, W. Zhou, S. Wang, Y. Zheng, W. Wei, and L. Chen, Opt. Lett. **41**, 4907 (2016).
[44] A. F. Mayadas and M. Shatzkes, Phys. Rev. B **1**, 1382 (1970).
[45] C. C. Tsuei, Phys. Rev. Lett. **57**, 1943 (1986).
[46] O. Gunnarsson, M. Calandra, and J. E. Han, Rev. Mod. Phys. **75**, 1085 (2003).
[47] X. Zhen, T. J. Huffman, X. Peng, A. J. Hollingshad, D. J. Brooker, N. E. Penthorn, M. M. Qazilbash, S. R. Saha, T. Drye, C. Roncaioli, and J. Paglione, Phys. Rev. B **94**, 064514 (2016).
[48] D. A. Tsukanov, M. V. Ryzhkova, D. V. Gruznev, O. A. Utas, V. G. Kotlyar, A. V. Zotov, and A. A. Saranin, Nanotechnology **19**, 245608 (2008).
[49] S. S. Jung, T. Lutz, A. P. Bell, E. K. McCarthy, and J. J. Boland, Cryst. Growth Des. **12**, 3076 (2012).
[50] N. Benouatta, A. Mosser, and A. Bouabellou, Appl. Surf. Sci. **252**, 7572 (2006).
[51] L. D. L. S. Valladares, D. H. Salinas, A. B. Dominguez, D. A. Najarro, S. I. Khondaker, T. Morelians, C. H. W. Barnes, J. A. Aguiar, and Y. Majima, Thin Solid Films **520**, 6368 (2012).
[52] H. Reddy, U. Guler, K. Chaudhuri, A. Dutta, A. V. Kildishev, V. M. Shalaev, and A. Boltasseva, ACS Photonics **4**, 1083 (2017).
[53] P. L. Bach, S. R. Saha, K. Kirshenbaum, J. Paglione, and R. L. Greene, Phys. Rev. B **83**, 212506 (2011).
[54] P. B. Johnson and R. W. Christy, Phys. Rev. B **11**, 1315 (1975).
[55] S. T. Sundari, S. Chandra, and A. K. Tyagi, J. Appl. Phys **114**, 033515 (2013).